Theoretical analysis of light-inductive forces in scanning probe microscopy

Christian Girard
Laboratoire de Physique Moléculaire, Université de Franche Comté, 25030 Besançon Cedex, France

Alain Dereux
Institute for Studies in Interface Sciences, Facultés Universitaires Notre Dame de la Paix, Rue de Bruxelles 61, B-5000 Namur, Belgium

Olivier J. F. Martin
IBM Research Division, Zurich Research Laboratory, Säumerstrasse 4, CH-8803 Rüschlikon, Switzerland
(Received 18 October 1993)

When two objects of subwavelength size interact in the presence of a light beam, a spatially confined electromagnetic field arises in a small spatial region located at the immediate proximity of the particles. In scanning probe microscopy, such induced short-range interactions change the magnitude of the forces interacting between the probe tip and the substrate. Depending on the frequency of light excitation with respect to those of the gap modes associated with the tip-sample junction, these inductive forces act to pull the probe toward the surface. Such an effect can be used to record optical adsorption of various samples with an atomic-force microscope. In this paper we show that the accurate description of the physical processes responsible for these forces can be analyzed within the framework of the localized field-susceptibility method. Practical solutions for the light-inductive force were found by discretization of the probe apex in real space. All multiple interactions including reflections with a substrate of arbitrary profile were accounted for by self-consistent procedures. We can therefore present simulations performed on systems of experimental interest.

I. INTRODUCTION

Since the pioneering work of Rohrer[1] and Binnig,[2] scanning probe microscopies and related methods proved to be valuable tools for studying a large class of physical observables at the nanometer scale (e.g., light emission in confined geometry, fluorescence properties of localized molecular aggregates, localized plasmon resonances, etc.).[1-3] In atomic-force microscopy (AFM), the use of interaction forces at the nanometer scale to image surfaces of insulating materials was developed as a complementary tool to the scanning tunneling microscope (STM).[4-6] The resolution obtained with an AFM depends strongly on the kind of tip-sample interactions involved in recording the images, and various theoretical models were proposed.[7-10]

In another related technique called scanning near-field optical microscopy (SNOM), the radiation emitted from a nanodetector (e.g., pointed optical fiber, metallic subwavelength particles, micropipette, etc.) is analyzed for different detector-sample configurations leading to subwavelength-resolved features lying on dielectric and metallic samples.[11-20] More recently, microfabricated probes for use in simultaneous optical near-field and force microscopy have been reported.[21,22] From such hybrid detectors, near-field images were directly compared to the topography displayed in the simultaneously recorded AFM images.

When an electromagnetic wave (e.g., laser light) is focused in the gap located between the probe tip and surface, various physical phenomena are expected. As described in Ref. 23 the absorption of light by the tip and sample can provoke a thermal expansion of the system, leading to possible optical-absorption spectroscopy for the sample. The electric field associated with the light beam can also produce an additional force between the detector and substrate. This inductive effect was already discussed in the context of scanning tunneling optical microscopy (STOM),[24] also called photon scanning tunneling microscopy (PSTM). Rough numerical estimations of this effect indicated that the order of magnitude of the inductive force is experimentally accessible. However, a detailed theoretical description of this effect which could predict accurately the magnitude and spatial distribution of inductive forces as a function of photon energy and tip-sample distance (or other geometrical and material parameters of both the probe and surface) is not yet available.

Recently,[25,26] we developed a theoretical approach to study the main features of the physical interaction between a thin probe tip and a corrugated surface. This study was based on a self-consistent calculation of the coupling modes of the two interacting systems in terms of the field susceptibilities associated with the sample.[27] In the present work we adapt this framework in order to derive a general expression for the tip-sample inductive force. The paper is organized as follows. In Sec. II we derive the field susceptibility of a single corrugated surface from a Dyson-type equation.[28] This response function is the key quantity of our problem, and the use of Dyson's equation to build it avoids the boundary condition problem. Using this field susceptibility of the isolat-

ed surface, a whole quantum electrodynamical treatment of the tip-substrate energy interaction in the presence of an external field is performed in Sec. III and final expressions of the concomitant forces are discussed. Experimentally relevant applications are proposed in Sec. IV.

II. FIELD SUSCEPTIBILITY OF A CORRUGATED SURFACE

The investigation of the electromagnetic response of rough surfaces was the subject of many previous theoretical works. For example, this problem was treated in Refs. 29 using a set of integral equations expressed in reciprocal space. Corrections to the results for a perfectly plane surface were obtained in terms of the Fourier transform of a smooth corrugation function $z=\eta(x,y)$ defining the weakly corrugated surface of the solid. However, such an approach is inadequate for studying awkward surface corrugations such as those encountered in scanning probe experiments. Moreover, it appears in this context that both mesoscopic and nanometric regimes are often undissociable, particularly when a probe tip is approached for local detection. For these reasons we preferred to adopt a real-space representation in which the defect lying on the substrate was built from a self-consistent procedure which avoided the usual boundary conditions on the surface of the defect.

The field susceptibility $\mathbf{S}(\mathbf{r},\mathbf{r}',\omega)$ of a material system reveals how a dipolar source field is modified at the proximity of the surface limiting this system.[27] In a general quantum description, this response function can be expressed in terms of the matrix elements of the field operator associated with the system of interest. The deduction of the response field of the solid to an arbitrary fluctuating dipole moment $\mathbf{m}_0(\omega)$ is another way of deriving this susceptibility.[27] In this section, we present a self-consistent calculation of this dyadic tensor $\mathbf{S}(\mathbf{r},\mathbf{r}',\omega)$ for a perfectly planar surface supporting localized defects of arbitrary shapes (see Fig. 1). In the first step we define

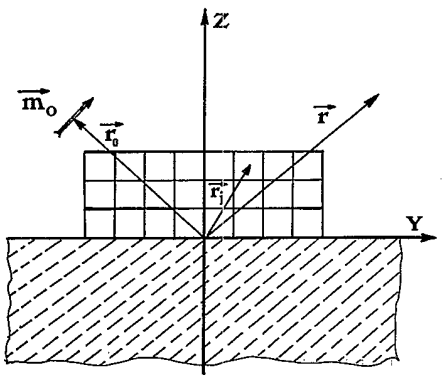

FIG. 1. Schematic illustration of a three-dimensional parallelepipedic surface defect lying on a flat surface (the reference system). The system is submitted to a pointlike dipolar excitation $\mathbf{m}_0$ located at the position $\mathbf{r}_0$. The surface defect is discretized with a set of n elementary cells located at the various positions $\mathbf{r}_j$.

the zero-order field, i.e., the field emitted by the fluctuating dipole $\mathbf{m}_0(\omega)$ located above the perfectly planar surface at the position $\mathbf{r}_0=(x_0,y_0,z_0)$:

$$\mathbf{e}_0(\mathbf{r},\omega)=\mathbf{s}_0(\mathbf{r},\mathbf{r}_0,\omega)\cdot\mathbf{m}_0(\omega)\ , \tag{1}$$

where the dyadic tensor $\mathbf{s}_0(\mathbf{r},\mathbf{r}_0,\omega)$ represents the field susceptibility of the planar surface (the reference system in our case). Various analytical forms for this response function are given explicitly in Ref. 27.

In the presence of the external field $\mathbf{e}_0(\mathbf{r},\omega)$ the microscopic components located inside the surface corrugation acquire fluctuating multipole moments which are perturbed by the surrounding dielectric. The resulting self-consistent electric field verifies the following implicit Lippmann-Schwinger[25,26] equation:

$$\mathbf{E}(\mathbf{r},\omega)=\mathbf{s}_0(\mathbf{r},\mathbf{r}_0,\omega)\cdot\mathbf{m}_0(\omega)+\int\int\mathbf{s}_0(\mathbf{r},\mathbf{r}',\omega)\cdot\chi_s(\mathbf{r}',\mathbf{r}'',\omega)\mathbf{E}(\mathbf{r}'',\omega)d\mathbf{r}'d\mathbf{r}''\ . \tag{2}$$

In this integral equation, the response function $\chi_s(\mathbf{r}',\mathbf{r}'',\omega)$ defines the linear susceptibility associated with the surface corrugation. If one assumes a local response for this perturbation, it is possible to relate χ_s to the local dielectric constant $\epsilon_s(\omega)$ of the surface defect:

$$\chi_s(\mathbf{r}',\mathbf{r}'',\omega)=\frac{[\epsilon_s(\omega)-1]}{4\pi}\delta(\mathbf{r}'-\mathbf{r}'')\ . \tag{3}$$

Such an approximation wipes out the integral over $\mathbf{r}''$, and is valid to deal with mesoscopic corrugations occurring in the context of local probe microscopies since it is well known that the macroscopic dielectric constant $\epsilon_s(\omega)$ does not need to be modified for particle sizes above 5 nm.[30] The survival internal occurring in (2) can then be performed by discretization in Cartesian space.[25,26] This leads to

$$\mathbf{E}(\mathbf{r},\omega)=\mathbf{s}_0(\mathbf{r},\mathbf{r}_0,\omega)\cdot\mathbf{m}_0(\omega)+\frac{[\epsilon_s(\omega)-1]}{4\pi}\sum_{j=1}^{n}W_j\mathbf{s}_0(\mathbf{r},\mathbf{r}_j,\omega)\cdot\mathbf{E}(\mathbf{r}_j,\omega)\ , \tag{4}$$

where W_j represents the volume of the jth discretized element in the surface corrugation. Note that the discretization of the surface defect is just a numerical procedure to take mesoscopic objects of arbitrary shape into account. The set of vectors $\{\mathbf{E}(\mathbf{r}_j,\omega)\}$ can be determined by a standard linear algebra procedure. Thus by setting $\mathbf{r}=\mathbf{r}_i$ in Eq. (4) one obtains the following matrix equation to be solved numerically:

$$\mathcal{F}(\omega)=\mathcal{A}(\omega)\bullet\mathcal{F}_0(\omega)\ , \tag{5}$$

where the symbol $\bullet$ indicates a total contraction on both Cartesian indexes and positions of discretized elements. Moreover $\mathcal{F}(\omega)$ and $\mathcal{F}_0(\omega)$ are two supervectors defined by

$$\mathcal{F}(\omega)=\{\mathbf{E}(\mathbf{r}_1,\omega);\mathbf{E}(\mathbf{r}_2,\omega);\ldots;\mathbf{E}(\mathbf{r}_n,\omega)\} \tag{6}$$

and

$$\mathcal{F}_0(\omega)=\mathcal{S}_0^t(\mathbf{r}_0,\omega)\cdot\mathbf{m}_0(\omega)\ , \tag{7}$$

where $\mathcal{S}_0^t(\mathbf{r}_0,\omega)$ is a supertensor given by

$$\mathcal{S}_0^t(\mathbf{r}_0,\omega)=\{\mathbf{s}_0(\mathbf{r}_1,\mathbf{r}_0,\omega);s_0(\mathbf{r}_2,\mathbf{r}_0,\omega);\ldots;s_0(\mathbf{r}_n,\mathbf{r}_0,\omega)\}\ . \tag{8}$$

In Eq. (5), the $(3n\times 3n)$ matrix $\mathcal{A}$ is built from different components taken by the field susceptibility $\mathbf{s}_0$ for all possible couples of position vectors $\{\mathbf{r}_i,\mathbf{r}_j\}$:

$$\mathcal{A}(\omega)=\left[\mathbf{I}-\frac{[\epsilon_s(\omega)-1]}{4\pi}\mathcal{B}(\omega)\right]^{-1}\ , \tag{9}$$

where $\mathbf{I}$ represents the identity tensor, and $\mathcal{B}(\omega)$ is the $(3n\times 3n)$ matrix defined by

$$\mathcal{B}(\omega)=\begin{bmatrix} W_1\mathbf{s}_0(\mathbf{r}_1,\mathbf{r}_1,\omega) & W_1\mathbf{s}_0(\mathbf{r}_1,\mathbf{r}_2,\omega) & \cdots & W_1\mathbf{s}_0(\mathbf{r}_1,\mathbf{r}_n,\omega) \\ W_2\mathbf{s}_0(\mathbf{r}_2,\mathbf{r}_1,\omega) & W_2\mathbf{s}_0(\mathbf{r}_2,\mathbf{r}_2,\omega) & \cdots & W_2\mathbf{s}_0(\mathbf{r}_2,\mathbf{r}_n,\omega) \\ \cdots & \cdots & \cdots & \cdots \\ \cdots & \cdots & \cdots & \cdots \\ W_n\mathbf{s}_0(\mathbf{r}_n,\mathbf{r}_1,\omega) & W_n\mathbf{s}_0(\mathbf{r}_n,\mathbf{r}_2,\omega) & \cdots & W_n\mathbf{s}_0(\mathbf{r}_n,\mathbf{r}_n,\omega) \end{bmatrix}\ . \tag{10}$$

This matrix contains all the dynamical and structural information about the surface defect when it interacts with the reference system. The diagonal terms describe the direct coupling between each discretized element and the substrate, while the off-diagonal terms are responsible for the interactions between these elements. Note that when the number n remains finite, the self-consistent equation (5) can be solved exactly. It is then possible to obtain the amplitudes of the effective fields $\mathbf{E}(\mathbf{r}_j,\omega)$. Furthermore when the size of the dynamical square matrix $\mathcal{A}(\omega)$ remains reasonable ($n\leq 500$), it is possible to derive accurate numerical solutions for the effective-field distribution contained in the supervector $\mathcal{F}(\omega)$. It is then a simple matter to obtain a general expression for the response field $\mathbf{E}(\mathbf{r},\omega)$ defined in (4). Substitution of Eqs. (5) and (7) into (4) leads to

$$\mathbf{E}(\mathbf{r},\omega)=\mathbf{s}_0(\mathbf{r},\mathbf{r}_0,\omega)\cdot\mathbf{m}_0(\omega)+\mathcal{S}_0(\mathbf{r}_0,\omega)\bullet\Lambda(\omega)\bullet\mathcal{A}(\omega)\bullet\mathcal{S}_0^t(\mathbf{r}_0,\omega)\cdot\mathbf{m}_0(\omega)\ , \tag{11}$$

where $\Lambda(\omega)$ is a block-diagonal matrix built from dynamical dipolar polarizibilities associated with each microsystem:

$$\Lambda(\omega)=\frac{\epsilon_s(\omega)^{-1}}{4\pi}\begin{bmatrix} W_1 & 0 & 0 & 0 & 0 & 0 & \cdots & 0 \\ 0 & W_1 & 0 & 0 & 0 & 0 & \cdots & 0 \\ 0 & 0 & W_1 & 0 & 0 & 0 & \cdots & 0 \\ 0 & 0 & 0 & W_2 & 0 & 0 & \cdots & 0 \\ 0 & 0 & 0 & 0 & W_2 & 0 & \cdots & 0 \\ 0 & 0 & 0 & 0 & 0 & W_2 & \cdots & 0 \\ 0 & 0 & 0 & 0 & 0 & 0 & \cdots & W_n \end{bmatrix} \tag{12}$$

and

$$\mathcal{S}_0(\mathbf{r}_0,\omega)=\{\mathbf{s}_0(\mathbf{r}_0,\mathbf{r}_1,\omega);\mathbf{s}_0(\mathbf{r}_0,\mathbf{r}_2,\omega);\ldots;\mathbf{s}_0(\mathbf{r}_0,\mathbf{r}_n,\omega)\}\ . \tag{13}$$

Let us recall that in the present description the surface defect is assumed to be homogeneous and isotropic. In Eq. (11), the response field $\mathbf{E}(\mathbf{r},\omega)$ is linear with respect to the external dipole moment $\mathbf{m}_0(\omega)$. Consequently the dyadic tensor connecting these two vectors is merely the field susceptibility of the system:

$$\mathbf{S}(\mathbf{r},\mathbf{r}',\omega)=\mathbf{s}_0(\mathbf{r},\mathbf{r}',\omega)+\mathcal{S}_0(\mathbf{r}',\omega)\bullet\Lambda(\omega)\bullet\mathcal{A}(\omega)\bullet\mathcal{S}_0^t(\mathbf{r}',\omega)\ . \tag{14}$$

Equation (14) establishes a simple and compact relation between the field susceptibility of a reference system (for example, the perfectly plane surface of a solid) and a more complex system displaying surface defects of arbitrary profile. Such a general equation is similar to the Dyson's equation currently used in the electronic Green's-function theory.[31] The many-body character of the interactions between the discretized elements is included in the matrix product $\Lambda(\omega)\bullet\mathcal{A}(\omega)$. Notice that, when the mesoscopic surface defect is replaced by a single polarizable center (an atomic or a molecule for example), the matrix $\Lambda(\omega)\bullet\mathcal{A}(\omega)$ reduces to a (3×3) diagonal matrix. In this particular case the general Eq. (14) can be solved analytically.[28]

III. COUPLED MODES OF THE TIP-SAMPLE SYSTEM

A. Model and basic equations

The application of an external field $\mathbf{E}_0(\mathbf{r},\omega)$ (e.g., a laser beam) to the corrugated surface creates a resulting electric field $\mathcal{E}_0(\mathbf{r},\omega)$ in the vicinity of the interface. As expected, this field is modified when a probing tip approaches the substrate. To obtain the new field distribution $\mathcal{E}(\mathbf{r},\omega)$ inside the probe-sample system, one needs to solve again an implicit integral equation

$$\mathcal{E}(\mathbf{r},\omega)=\mathcal{E}_0(\mathbf{r},\omega)+\int \mathbf{S}(\mathbf{r},\mathbf{r}',\omega)\cdot\chi_p(\mathbf{r}',\omega)\cdot\mathcal{E}(\mathbf{r}',\omega)d\mathbf{r}' , \tag{15}$$

where the integral extends on the volume occupied by the probe tip, and χ_p describes its linear susceptibility. Once again, if one assumes a local response for the material composing the detector, this equation can be solved with a discretization procedure similar to the one used in Sec. II to derive the dyadic tensor $\mathbf{S}(\mathbf{r},\mathbf{r}',\omega)$. This leads to the following set of linear coupled equations:

$$\mathbf{V}(\omega)=\mathcal{N}(\omega)\bullet\mathbf{V}_0(\omega) , \tag{16}$$

where $\mathbf{V}(\omega)$ and $\mathbf{V}_0(\omega)$ are two supervectors defined by

$$\mathbf{V}(\omega)=\{\mathcal{E}(\mathbf{R}_1,\omega);\mathcal{E}(\mathbf{R}_2,\omega);\ldots;\mathcal{E}(\mathbf{R}_m,\omega)\} \tag{17}$$

and

$$\mathbf{V}_0(\omega)=\{\mathcal{E}_0(\mathbf{R}_1,\omega);\mathcal{E}_0(\mathbf{R}_2,\omega);\ldots;\mathcal{E}_0(\mathbf{R}_m,\omega)\} \tag{18}$$

and

$$\mathcal{N}(\omega)=[\mathbf{I}-\mathcal{M}(\omega)]^{-1} , \tag{19}$$

where m represents the number of discretization points used to treat the probe tip. In Eq. (19), the matrix $\mathcal{M}(\omega)$ is built from different components taken by the field susceptibility $\mathbf{S}$ for all possible couples of position vectors $\{\mathbf{R}_l,\mathbf{R}_k\}$ defined inside the tip:

$$\mathcal{M}(\omega)=\chi_p(\omega)\begin{bmatrix} \eta_1\mathbf{S}(\mathbf{R}_1,\mathbf{R}_1,\omega) & \eta_1\mathbf{S}(\mathbf{R}_1,\mathbf{R}_2,\omega) & \cdots & \eta_1\mathbf{S}(\mathbf{R}_1,\mathbf{R}_m,\omega) \\ \eta_2\mathbf{S}(\mathbf{R}_2,\mathbf{R}_1,\omega) & \eta_2\mathbf{S}(\mathbf{R}_2,\mathbf{R}_2,\omega) & \cdots & \eta_2\mathbf{S}(\mathbf{R}_2,\mathbf{R}_m,\omega) \\ \cdots & \cdots & \cdots & \cdots \\ \cdots & \cdots & \cdots & \cdots \\ \eta_m\mathbf{S}(\mathbf{R}_m,\mathbf{R}_1,\omega) & \eta_m\mathbf{S}(\mathbf{R}_m,\mathbf{R}_2,\omega) & \cdots & \eta_m\mathbf{S}(\mathbf{R}_m,\mathbf{R}_m,\omega) \end{bmatrix} , \tag{20}$$

where η_j is the weight attributed to the jth discretized element located inside the detector.

Dispersion equation

Let us note that if the source field $\mathcal{E}_0$ contained in the supervector $\mathbf{V}_0(\omega)$ vanishes, we find the following eigenvalue:

$$\mathbf{V}(\omega)=\mathcal{M}(\omega)\bullet\mathbf{V}(\omega) . \tag{21}$$

The allowed coupled modes are then given by the solutions for the dispersion equation

$$\mathcal{D}(\omega)=\det[\mathbf{I}-\mathcal{M}(\omega)]=0 . \tag{22}$$

The positive roots of this equation determine the possible eigenfrequencies of the tip-sample junction for a given spatial configuration. The influence of surface roughness on these modes was included in the propagator $\mathbf{S}$ derived in Sec. II.

Effective field inside the substrate

It is now possible to derive a general expression for the optical electric field inside both the surface defect and the reference system. In fact, from Eq. (15) the knowledge of both the effective field distribution inside the tip [cf. Eq. (17)] and the propagator $\mathbf{S}$ is sufficient to describe the resulting field inside the substrate. This leads to

$$\mathcal{E}(\mathbf{r},\omega)=\mathcal{E}_0(\mathbf{r},\omega)+\sum_{i=1}^{m}\eta_i\chi_p(\omega)\mathbf{S}(\mathbf{r},\mathbf{R}_i,\omega)\cdot\mathcal{E}(\mathbf{R}_i,\omega) \tag{23}$$

for any point $\mathbf{r}$ located inside the reference system, and to

$$\mathcal{E}(\mathbf{r}_j,\omega)=\mathcal{E}_0(\mathbf{r}_j,\omega)+\sum_{i=1}^{m}\eta_i\chi_p(\omega)\mathbf{S}(\mathbf{r}_j,\mathbf{R}_i,\omega)\cdot\mathcal{E}(\mathbf{R}_i,\omega) \tag{24}$$

for each discretized points located inside the corrugation surface.

We note that the above procedure avoided matching boundary conditions on the surface of the probe tip. They are automatically satisfied by the self-consistency of the integral equation (15). The boundary conditions at infinity (Sommerfeld radiation condition) are guaranteed by the asymptotic behavior of the propagator $\mathbf{S}(\mathbf{r},\mathbf{r}',\omega)$, which generates spherical waves at large distance from the field sources.

B. The tip-sample force in the noncontact regime

When the probing tip is scanned across the surface at a height sufficiently large to ensure that no overlap of the electrons wave functions occurs, the long-range interaction energy in the absence of permanent charges is composed of two contributions:

$$U(\mathbf{R}_p)=U_{\text{vdw}}(\mathbf{R}_p)+U_{\text{ind}}(\mathbf{R}_p) . \tag{25}$$

The first one is the dispersion van der Waals energy. The existence of such long-range forces can be inferred from the correlation between fluctuations of the charge densities inside the probe tip and substrate. According to the van der Waals force theory,[27] the knowledge of the dispersion equation (22) is sufficient for determining $U_{\rm vdw}(\mathbf{R}_p)$:

$$U_{\rm vdw}(\mathbf{R}_p)=\frac{\hbar}{2\pi}\int_0^\infty \ln\mathcal{D}(iu)du \ . \tag{26}$$

After substituting Eq. (22) into Eq. (26), this energy can be written

$$U(\mathbf{R}_p)=\frac{\hbar}{2\pi}\int_0^\infty \ln[\mathbf{I}-\mathcal{M}(iu)]du \ . \tag{27}$$

Let us note that in the context of the dispersion interactions the presence of the integral on imaginary frequency eliminates all resonance phenomena. In this situation each matrix element of $\mathcal{M}(iu)$ remains small with respect to unity. It is then possible to obtain an accurate description of $U_{\rm vdw}(\mathbf{R}_p)$ by applying the following expansion:

$$U(\mathbf{R}_p)=-\frac{\hbar}{2\pi}\sum_{q=1}^{\infty}\frac{1}{q}\int_0^\infty \mathrm{Tr}[\mathcal{M}^{(q)}(iu)]du \ , \tag{28}$$

where the symbol $\mathcal{M}^{(q)}$ represents the matrix product of mth order. It may be seen that the first term ($m=1$) corresponds to the direct coupling between each element inside the probe tip and the surface, while the other terms account for the many-body effects.

In Eq. (25) the second contribution represents the light-inductive energy.[24] The calculation of this quantity requires the form of the external field $\mathbf{E}_0(\mathbf{r},t)$ to be specified. In the present work we will restrict our discussion to the case of an external monochromatic field of frequency ω_0. In this case the Fourier transform can be written

$$\mathbf{E}_0(\mathbf{r},\omega)=\pi\delta(\omega-\omega_0)\mathbf{f}(\mathbf{r})+\pi\delta(\omega+\omega_0)\mathbf{f}^*(\mathbf{r}) \ , \tag{29}$$

where the analytical form of the spatial function $\mathbf{f}(\mathbf{r})$ depends on the location of the laser beam (e.g., internal or external configurations). With such a monochromatic source field it is straightforward to demonstrate that the time-dependent effective field $\mathcal{E}(\mathbf{r},\omega)$ inside the probe-sample junction can be expressed by

$$\mathcal{E}(\mathbf{r},t)=\tfrac{1}{2}\{e^{i\omega_0 t}\mathbf{\Gamma}(\mathbf{r},\omega_0)+e^{-i\omega_0 t}\mathbf{\Gamma}^*(\mathrm{rc},\omega_0\} \ . \tag{30}$$

The value of the vector function $\mathbf{\Gamma}$ depends on the location of the position vector $\mathbf{r}$ in the system. Inside the probe tip it is given by

$$\mathbf{\Gamma}(\mathbf{R}_i,\omega_0)=\sum_{k=1}^{m}\mathcal{N}_{i,k}(\omega_0)\cdot\mathcal{E}_0(\mathbf{R}_k,\omega_0) \tag{31}$$

(as described in Sec. III A, the vector $\mathcal{E}_0$ represents the effective field in the absence of the probe); and inside the substrate it is given by

$$\mathbf{\Gamma}(\mathbf{r},\omega_0)=\mathcal{E}_0(\mathbf{r},\omega_0)+\sum_{i=1}^{m}\sum_{k=1}^{m}\eta_i\chi_p(\omega_0)\mathbf{S}(\mathbf{r},\mathbf{R}_i,\omega_0)\times\mathcal{N}_{i,k}(\omega_0)\cdot\mathcal{E}_0(\mathbf{R}_k,\omega_0) \ , \tag{32}$$

where $\mathbf{r}=\mathbf{r}_j$ inside the surface defect, and $\mathbf{r}=(x,y,z\le 0)$ is a point located inside the reference system. From these equations it is now possible to derive the time-dependent electrical polarization inside the tip-sample junction:

$$\mathcal{P}_\alpha(\mathbf{r},t)=\tfrac{1}{2}\{\chi_\alpha(\omega_0)e^{i\omega_0 t}\mathbf{\Gamma}(\mathbf{r},\omega_0)+\mathrm{c.c.}\} \ . \tag{33}$$

In this relation the index α takes the values p and s in the probe and substrate, respectively. Let us note that this induced polarization density is, by means of the function $\mathbf{\Gamma}$, a functional of the external field $\mathbf{E}_0$. Hence, when this field passes from zero to the finite value $\mathbf{E}_0$, the system acquires a light-inductive energy given by the relation

$$U_{\rm ind}(\mathbf{R}_p)=-\tfrac{1}{2}\sum_\alpha\left\langle\int_v\mathcal{P}_\alpha(\mathbf{r},t)\cdot\mathcal{E}(\mathbf{r},t)d\mathbf{r}\right\rangle_t \ , \tag{34}$$

where the integral has to be performed on both the volume v occupied by the probe and sample. The brackets indicate that the time average must be taken. Using Eqs. (29)–(33), the relation (34) can be split into two parts:

$$U_{\rm ind}(\mathbf{R}_p)=U_{\rm ind}^{(p)}(\mathbf{R}_p)+U_{\rm ind}^{(s)}(\mathbf{R}_p) \ . \tag{35}$$

The first term $U_{\rm ind}^{(p)}$ describes the inductive energy experiences by the detector. This quantity can be expanded on the discretization grid $\{\mathbf{R}_i\}$ previously used to solve the self-consistent field (see Sec. III A). Such a procedure leads to

$$U_{\rm ind}^{(p)}(\mathbf{R}_p)=-\tfrac{1}{8}\sum_{i=1}^{m}\{\eta_i\chi_p(\omega_0)\mathbf{\Gamma}(\mathbf{R}_i,\omega_0)\times\mathbf{\Gamma}^*(\mathbf{R}_i,\omega_0)+\mathrm{c.c.}\} \ . \tag{36}$$

Using a similar procedure, the second term $U_{\rm ind}^{(s)}$ associated with the sample can be expressed as

$$U_{\rm ind}^{(s)}(\mathbf{R}_p)=-\tfrac{1}{8}\sum_{j=1}^{n}[W_j\chi_s(\omega_0)\mathbf{\Gamma}(\mathbf{r}_j,\omega_0)\cdot\mathbf{\Gamma}^*(\mathbf{r}_j,\omega_0)+\mathrm{c.c.}]-\tfrac{1}{8}\int\int dx\,dy\int_{-\infty}^{0}dz[\chi_s(\omega_0)\mathbf{\Gamma}(\mathbf{r},\omega_0)\cdot\mathbf{\Gamma}^*(\mathbf{r},\omega_0)+\mathrm{c.c.}] \ , \tag{37}$$

where the first part is simply the contribution originating from the surface defect. According to the discretization procedure described above, this quantity reappears as a summation over all the elementary cells used to treat the three-dimensional surface defect (cf. Fig. 2). Finally the second term in Eq. (37) corresponds to the inductive energy gained by the reference system in the presence of the probing tip.

In order to clarify the subsequent discussion, it is important to remark that the two contributions [Eqs. (36) and (37)] associated with the light-inductive energy are expressed in a very concise way by the field amplitude $\Gamma(\mathbf{r},\omega_0)$ [see Eqs. (31) and (32)]. As indicated in the pair of relations (31) and (32) for a given spatial tip-sample configuration and for a given frequency ω_0, Γ displays resonances when

$$\mathrm{Re}[\det(\mathcal{N}^{-1}(\omega_0))]=0 \ . \tag{38}$$

In particular, for a pointed metallic tip placed above a metallic substrate this resonance can occur in the optical range before the tip touches the sample surface. Such resonant effects were recently observed by generating localized plasmons on a spherical metallic detector approaching a surface. In the near-field zone (about 100 nm from the surface) extremely narrow resonance peaks versus the approach distance were recorded.[32] In the present case, such gap modes could also generate specific resonances phenomenon in the inductive force characteristic. This differs from the van der Waals force characteristic [see Eq. (27)], in which the imaginary frequency integration damps all resonance phenomena.

IV. APPLICATION TO SPECIFIC CONFIGURATIONS

The main component of all scanning probe microscopes is the nanoprobe which records the relevant physically observable phenomena for a given spatial configuration (e.g., tunneling current, interacting forces, electromagnetic field). In the context of near-field experiments coupled with force sensor devices, two different kinds of optical probes have already been investigated. The first class is obtained by mechanical pulling and chemical etching of both monomode or multimode optical fibers.[3,4] the second type are microfabricated SiN probes currently used in AFM: they are composed of a pyramid apex integrated on a microcantilever.[21,22] In this case the tip extremity is a tetrahedrally shaped protrusion where four faces and four sharp edges converge in

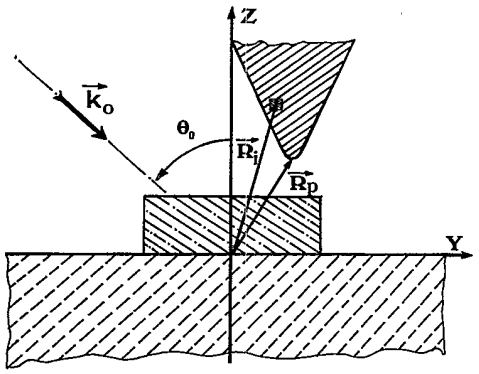

FIG. 2. Geometry of an experimental scanning probe device lit in external reflection. The wave vector $\mathbf{K}_0$ is located in the (YOZ) plane, and the incident angle is labeled θ_0. The vector $\mathbf{R}_P=(X_P,Y_P,Z_P)$ defines the detector apex position, and $\mathbf{R}_i$ characterizes the location of given volume element inside the probe tip.

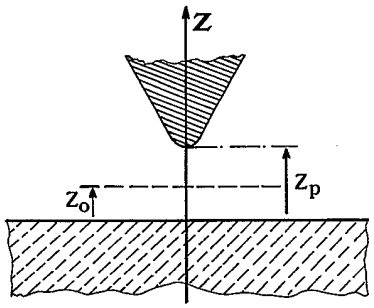

FIG. 3. Geometry used in the numerical application of Sec. IV. The shape of the tip is tetrahedral like those currently used in scanning force microscopy. The aperture angle used in our simulation is chosen equal to 90°. Z_p represents the tip-sample approach distance, and Z_0 defines a plane located inside the gap.

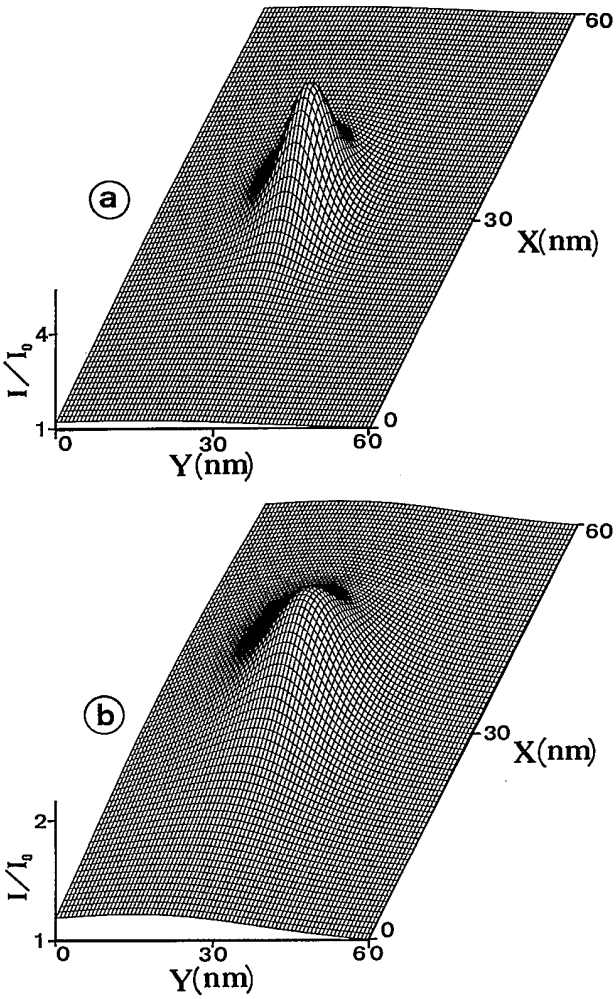

FIG. 4. Perspective view of the normalized electric-field intensity distribution I/I_0 inside the tip-sample junction calculated in a plane $z=Z_0$ parallel to the surface. The zeroth-order solution in the half-space $(z>0)$ is the superposition of an incident plane wave and the reflected field from the surface. The incident angle $\theta_0=75°$, and the calculation has been performed with a tetrahedral tip of height $H=100$ nm. The curvature radius of the tip end is equal to 7.5 nm. (a) $Z_p=5$ nm; $Z_0=2.5$ nm. (b) $Z_P=15$ nm; $Z_0=7.5$ nm.

a common tip ending with a small curvature radius r_{pr} (1 nm $\leq r_{pr} \leq 50$ nm). In our application, we considered such a tetrahedral tip apex facing a perfectly plane surface (cf. Fig. 3). This choice avoided the complexity introduced by the real profile of the substrate. Nevertheless, it retained the main characteristics of the physical processes investigated in this paper. A more complete simulation based on the entire formalism detailed in Secs. II and III is planned for a forthcoming paper.

A. Field distribution in the tip-sample junction

The tip chosen to calculate the light-inductive force $U_{\text{ind}}(\mathbf{R}_p)$ [cf. Eqs. (35), (36), and (37)] was a pyramid (height H and aperture angle $\alpha=90°$) with an optical index n_{pr} varying between 1.5 and 2.2. Moreover, for the computation we considered a discretization grid built from a Cartesian mesh consisting of six layers of grid points organized in a succession of square layers parallel to the sample surface. Furthermore we will restrict our application to the external reflection configuration described in Fig. 2. In this case, the zeroth order excitation field $\mathbf{E}_0(\mathbf{r},\omega)$ (cf. Sec. III A) above the surface is the sum of an incident plane wave of frequency ω_0 and a reflected wave by the substrate. In the p-polarized operating mode this field is written as

$$\mathbf{E}_0(\mathbf{r},\omega)=\pi E_0\{\mathbf{f}(\mathbf{r})\delta(\omega-\omega_0)+\mathbf{f}^*(\mathbf{r})\delta(\omega+\omega_0)\}\ , \tag{39}$$

with

$$f_x(\mathbf{r})=0\ , \tag{40}$$

$$f_y(\mathbf{r})=[e^{-i\mathbf{k}_0\cdot\mathbf{r}}-R_p e^{-i\mathbf{k}_1\cdot\mathbf{r}}]\cos(\theta_0)\ , \tag{41}$$

$$f_z(\mathbf{r})=[e^{-i\mathbf{k}_0\cdot\mathbf{r}}+R_p e^{-i\mathbf{k}_1\cdot\mathbf{r}}]\sin(\theta_0)\ , \tag{42}$$

where E_0 represents the magnitude of the incident field, and R_P is the reflection coefficient of the sample; $\mathbf{k}_0$ and $\mathbf{k}_1$ are the wave vectors of the incident and reflected waves, respectively, while θ_0 represents the angle of incidence. We chose the configuration in which the vector $\mathbf{k}_0$ was parallel to the (YOZ) plane.

As illustrated by the pair of relations (36) and (37), the

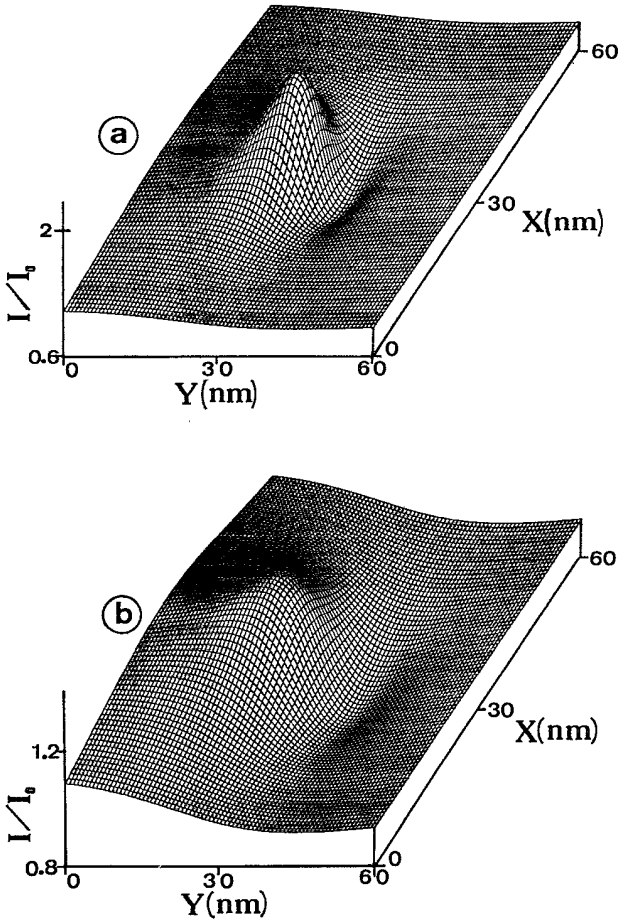

FIG. 5. Same as Fig. 4, except that the incident angle is $\theta_0=15°$.

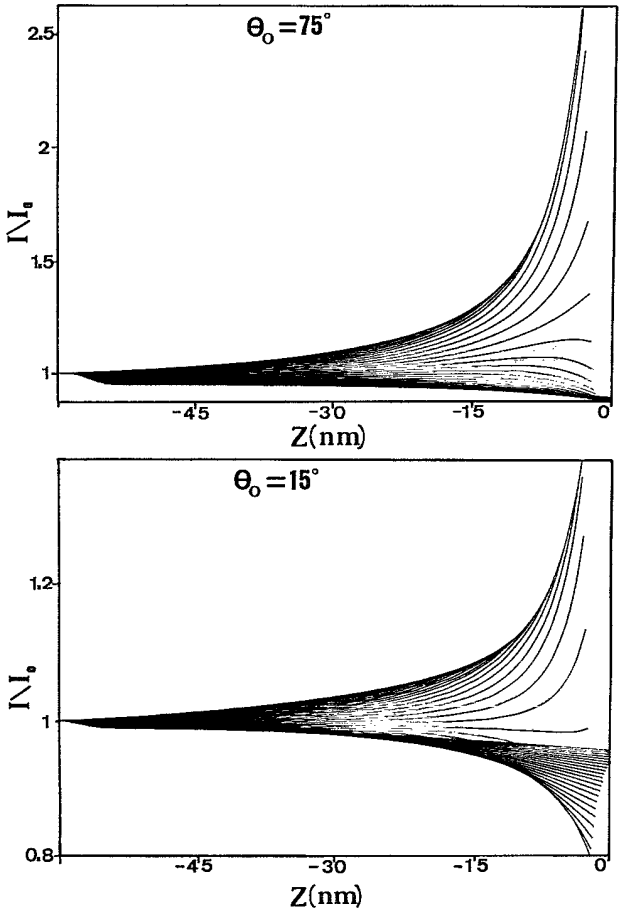

FIG. 6. Illustration of the variation of the normalized electric-field intensity (I/I_0) inside the substrate. The two sequences of curves show the variation of the intensity induced by the presence of the SFM tip. These curves have been calculated for different lateral positions Y spaced 2 nm apart along the surface. The parameters of the SFM tip are those of Figs. 4 and 5, and its position is $Z_p=5$ nm.

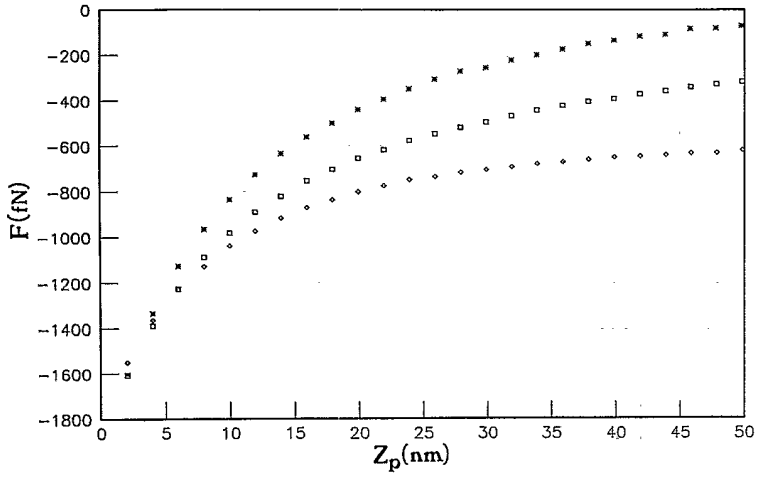

FIG. 7. Variation of the normal light inductive forces as a function of the approach distance Z_P (in fN). The calculation was performed with a tetrahedral tip of height $H=400$ nm, and of curvature radius $r_{pr}=40$ nm. ★, $\theta_0=56.5°$ (Brewster angle); □, $\theta_0=50°$; and ◇, $\theta_0=60°$.

magnitude of both the light-inductive energy and the concomitant normal force defined by

$$F_z=-\frac{\partial}{\partial Z_p}U_{\text{ind}} \tag{43}$$

depends on the magnitude of the self-consistent field $\Gamma(\mathbf{r},\omega)$ located around the tip-sample junction. As expected, the confined character of this field is responsible for the efficiency of the optical binding between the tip and substrate. In order to characterize the spatial extension of this confinement, we calculated the normalized electric field intensity $\eta=I/I_0$ inside the gap formed by the tip-sample interface (cf. Figs. 4 and 5). In this ratio, I_0 corresponds to the intensity calculated in the absence of the detector. These calculations have been performed with a tetrahedral tip of height $H=100$ nm and of optical index $n_{pr}=1.5$. We found that for an approach distance Z_P of about 5 nm, a very confined field occurs in the gap. Using a 7.5-nm-radius tip end we usually obtained less than 20-nm lateral extension for this field intensity. Moreover, in the external reflection configuration, the shape of the intensity maps calculated in the p-polarized mode depended dramatically on the incidence angle θ_0. A possible origin of this effect is the shadow introduced by the probe in th near-field zone. This situation occurred preferentially for small angles of incidence (cf. Fig. 5). In any case these simulations illustrated convincingly the optical confinement originating from the interfaces geometry.

We addressed the question of the decay of the normalized intensity $\eta=I/I_0$ induced by the detector inside the sample (see Fig. 6). This quantity could easily be derived from the results established in Sec. III B [see Eq. (32)]. As expected, knowledge of the spatial variation of $\eta(x,y,z)$ inside the substrate afforded some insight into the efficiency of the tip-sample coupling. It allowed us to define precisely a criterion to determine the range over which the threefold integral occurring in Eq. (37) must be performed. Sets of $\eta(z)$ curves are presented in Fig. 7 for a fixed position of the tip $\mathbf{R}_P=(0,0,5$ nm). These curves have been calculated for different lateral position y_k spaced 2 nm apart along the surface. Note that the extension of the field penetration inside the substrate is strongly limited and varies dramatically with respect to θ_0. It may be seen, for example, that for large incident angles the decay length is optimum just below the tip apex. Furthermore, the variation of the field induced under the surface occurs on a scale fixed by the probe tip size.

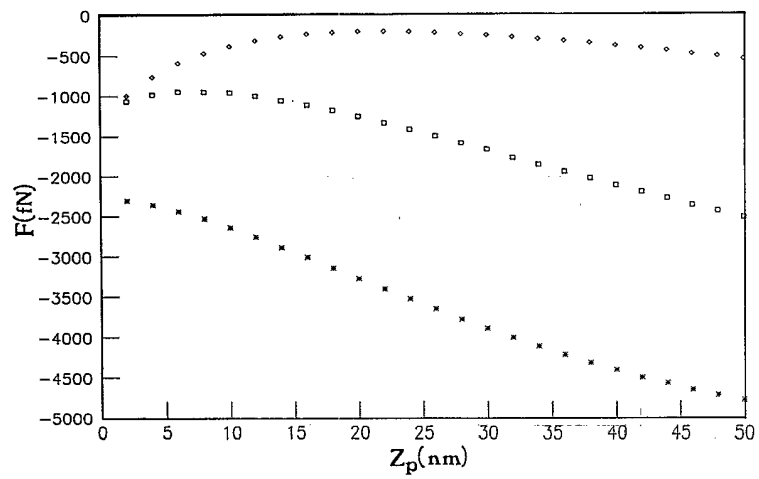

FIG. 8. Same as Fig. 7, but with ★, $\theta_0=10°$; □, $\theta_0=20°$; and ◇, $\theta_0=30°$.

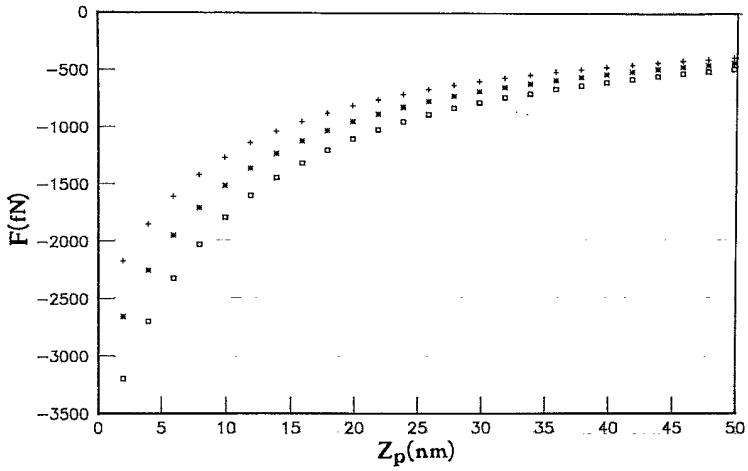

FIG. 9. Same as Fig. 7, but calculated with different values of the probe tip optical index: +, $n_{pr}=1.8$; ★, $n_{pr}=2$; and □, $n_{pr}=2.2$.

Indeed for a 100-nm-height tip, the ratio η is nearly equal to unity when $|z|$ is greater than about 60 nm.

B. The optical binding force

Having collected enough data about the spatial distribution of the confined optical field around the interface, it was possible to study numerically the behavior of the optical binding force F_z [see Eq. (43)]. As in Ref. 33, we assumed that the laser beam after focusing provided 2.2 W of mean power over a surface of 150 μm^2. From the knowledge of the function $U_{ind}(X_P, Y_P, Z_P)$, it was easy to obtain the normal light force. For a given spatial configuration ($X_P=0, Y_P=0$), U_{ind} was computed for a small number of points located around Z_P. The function U_{ind} was then fitted from these points by a polynomial in Z. We used five values of Z to fit $U_{ind}(z)$. The z-force component was calculated at point Z_p from this polynomial. In Figs. 7, 8, and 9, F_z is drawn as a function of the approach distance Z_P. The calculation took into account a tetrahedral tip of height $H=400$ nm terminated by curvature radius $r_{pr}=40$ nm. For a mean power of 15 mW/μm^2, the magnitude of the force varied within 2 and 5 pN when the tip was located in the immediate proximity of the sample. Such a force can be currently detected by using AFM resonant devices.[5] Furthermore, for a fixed sample-to-tip edge distance, F_z appeared to be very sensitive to the incident angle θ_0 (see Figs. 7 and 8). This light-polarization effect originates from a subtle competition between the interference pattern generated by the superposition of both incident and reflected waves and the optical near-field confined by the tip-sample interaction. Thus, as evidenced in Fig. 7, working in the vicinity of the incident Brewster angle appears to provide an interesting opportunity to observe the purely optical binding force alone. Finally, it is interesting to note the strong sensitivity of the magnitude of F_z with respect to the optical index of the detector (Fig. 9).

V. CONCLUSION

Using the field-susceptibility method we have proposed a theoretical analysis of physical mechanisms underlying the light-inductive forces occurring when a laser beam is focused in the gap formed by a thin probe tip and a corrugated surface. We have also detailed a numerical solution procedure that allows realistic geometries to be handled. The numerical applications discussed above illustrate optical confinement as it originates from the tip-sample geometry. Another interesting finding is that a very direct link exists between the spatial localization of the optical energy and the characteristics of the light-inductive force. Moreover, our simulations clearly indicated that working in the vicinity of the Brewster angle might be of experimental interest for recording the purely optical binding force between the two interacting systems. Finally the direct-space discretization procedure used to solve this coupled system may easily be adapted to the study of other experimental configurations (e.g., total internal reflection, coated metallic tip).

ACKNOWLEDGMENTS

We thank Dr. O. Marti and M. Hipp for interesting discussions. One of us (A.D.) gratefully acknowledges the Walloon Ministry for Research and Technology (Brussels) for financial support. The Laboratoire de Physique Moléculaire is Unité associée au Centre National de la Recherche Scientifique No. 772.

[1]H. Rohrer, Ultramicroscopy **42-44**, 1 (1992).
[2]G. Binnig, Ultramicroscopy **42-44**, 7 (1992); G. Binnig, C. F. Quate, and Ch. Gerber, Phys. Rev. Lett. **56**, 930 (1986); O. Marti, H. O. Ribi, B. Drake, T. R. Albrecht, C. F. Quate, and P. K. Hansma, Science **239**, 50 (1988).
[3]D. W. Pohl, Adv. Opt. Electron. Microsc. **12**, 243 (1991), and references therein.
[4]E. Meyer, Prog. Surf. Sci. **41**, 1 (1992).
[5]D. Sarid, *Scanning Force Microscopy* (Oxford University Press, New York, 1991).
[6]D. Rugar and P. Hansma, Phys. Today **43** (1), 23 (1990), and references therein.
[7]F. F. Abraham and I. P. Batra, Surf. Sci. **209**, L125 (1989); S. Ciraci, A. Baratoff, and I. P. Batra, Phys. Rev. B **41**, 2763

(1990); S. Ciraci, E. Tekman, M. Gökçsdag, I. P. Batra, and A. Baratoff, Ultramicroscopy **42-44**, 163 (1992).

[8]W. Zong, G. Overney, and D. Tomanek, Europhys. Lett. **15**, 49 (1991); G. Overney, D. Tomanek, W. Zang, Z. Sun, H. Miyazaki, S. D. Mahanti, and H. J. Güntherrodt, J. Phys. C **4**, 4233 (1992).

[9]C. Girard, Phys. Rev. B **43**, 8822 (1991); C. Girard, S. Maghezzi, and D. Van Labeke, Surf. Sci. **234**, 181 (1990).

[10]U. Hartmann, Phys. Rev. B **42**, 1541 (1990); **43**, 2404 (1991).

[11]E. Betzig, J. K. Trautman, T. D. Harris, J. S. Weiner, and R. L. Kostelak, Science **251**, 1468 (1991), and references therein.

[12]R. Reddick, R. J. Warmack, and T. J. Ferrel, Phys. Rev. B **39**, 767 (1989).

[13]D. Courjon, K. Sarayeddine, and M. Spajer, Opt. Commun. **71**, 23 (1989).

[14]J. A. Cline, H. Barshatzky, and M. Isaacson, Ultramicroscopy **38**, 299 (1991).

[15]N. F. Van Hulst, F. B. Segering, and B. Bolger, Opt. Commun. **87**, 212 (1992).

[16]K. Lieberman and A. Lewis, Ultramicroscopy **42-44**, 399 (1991).

[17]T. L. Ferrel, S. L. Sharp, and R. J. Warmack, Ultramicroscopy **42-44**, 408 (1991).

[18]F. de Fornel, L. Salomon, P. Adam, E. Bourillot, J. P. Goudonnet, and M. Neviere, Ultramicroscopy **42-44**, 422 (1992).

[19]M. Specht, J. D. Pedarnig, W. M. Heckl, and T. W. Hansch, Phys. Rev. Lett. **68**, 476 (1992).

[20]M. A. Paesler, P. J. Moyer, C. J. Jahncke, C. E. Johnson, R. C. Reddick, R. J. Warmick, and T. L. Ferrel, Phys. Rev. B **42**, 6750 (1990).

[21]F. Baida, D. Courjon, and G. Trebillon, in *Near Field Optics,* Vol. 8 of *NATO Advanced Study Institute Series E: Applied Sciences,* edited by D. W. Pohl and D. Courjon (Kluwer, Dordrecht, 1993), p. 71.

[22]N. F. van Hulst, M. H. P. Moers, O. F. J. Noordman, T. Faulkner, F. B. Segerink, K. O. van der Werf, B. G. de Grooth, and B. Bölger, Proc. SPIE **1639**, 36 (1992).

[23]M. Nonnenmacher and H. K. Wickramasinghe, Ultramicroscopy **42-44**, 351 (1992).

[24]F. Depasse and D. Courjon, Opt. Commun. **87**, 79 (1992).

[25]C. Girard, X. Bouju and A. Dereux, in *Near Field Optics* (Ref. 21), p. 199.

[26]A. Dereux, J. P. Vigneron, Ph. Lambin, and A. A. Lucas, Physica B **175**, 65 (1991).

[27]C. Girard and X. Bouju, J. Chem. Phys. **95**, 2056 (1991).

[28]C. Girard, A. Dereux, and O. J. F. Martin, Surf. Sci. **295**, 445 (1993).

[29]A. M. Marvin and F. Toigo, Phys. Rev. A **25**, 782 (1982); T. S. Rahman and A. A. Maradudin, Phys. Rev. B **21**, 504 (1980).

[30]C. F. Bohren and D. R. Huffman, *Absorption and Scattering of Light by Small Particles* (Wiley, New York, 1983).

[31]E. N. Economou, *Green's Functions in Quantum Physics,* 2nd ed. (Springer, Berlin, 1983).

[32]U. Ch. Fisher and D. W. Pohl, Phys. Rev. Lett. **62**, 458 (1989).

[33]M. M. Burns, J. M. Fournier, and J. A. Golovchenko, Phys. Rev. Lett. **63**, 1233 (1989).